HAL
open science

Tracking pores during solidification of a Ni-based superalloy using 4D synchrotron microtomography

Emeric Plancher, Pauline Gravier, Edouard Chauvet, Jean-Jacques Blandin, Elodie Boller, Guilhem Martin, Luc Salvo, Pierre Lhuissier

To cite this version:

Emeric Plancher, Pauline Gravier, Edouard Chauvet, Jean-Jacques Blandin, Elodie Boller, et al.. Tracking pores during solidification of a Ni-based superalloy using 4D synchrotron microtomography. Acta Materialia, 2019, 181, pp.1-9. 10.1016/j.actamat.2019.09.040 . hal-02402505

HAL Id: hal-02402505

https://hal.science/hal-02402505v1

Submitted on 4 Dec 2020

HAL is a multi-disciplinary open access archive for the deposit and dissemination of scientific research documents, whether they are published or not. The documents may come from teaching and research institutions in France or abroad, or from public or private research centers.

L'archive ouverte pluridisciplinaire **HAL**, est destinée au dépôt et à la diffusion de documents scientifiques de niveau recherche, publiés ou non, émanant des établissements d'enseignement et de recherche français ou étrangers, des laboratoires publics ou privés.

Tracking pores during solidification of a Ni-based superalloy using 4D synchrotron microtomography.

E. Plancher[1], P. Gravier[1], E. Chauvet[1], J.-J. Blandin[1], E. Boller[2], G. Martin[1,*], L. Salvo[1], P. Lhuissier[1,*]

1 Université Grenoble Alpes, CNRS UMR5266, Grenoble INP, Laboratoire SIMaP, 38000 Grenoble, France.

2 ESRF-The European Synchrotron, CS40220, 38043, Grenoble Cedex 9, France

*corresponding authors: guilhem.martin@simap.grenoble-inp.fr (G. Martin), pierre.lhuissier@simap.grenoble-inp.fr (P. Lhuissier)

Abstract

Time-resolved *in situ* microtomography is employed to track the nucleation and growth of individual pores during solidification of a commercial nickel-based superalloy. Three cooling rates (0.1, 0.5 and 1°C/s) are investigated to evaluate the effect of this key processing parameter on the formation of porosity. Phase contrast obtained with a coherent X-ray beam is used to visualize the evolution of dendritic structures in absence of a sufficient absorption contrast. Two mechanisms leading to shrinkage pores have been identified. The first mechanism (mechanism A) is associated with the coalescence of secondary dendrite arms at temperature during the early stages of solidification. The second mechanism (mechanism B) is related to insufficient liquid feeding in the interdendritic region during the last stages of solidification, at lower temperatures. A variation of cooling rate by a factor 2 does not affect the nucleation rate of pores generated through mechanism B. However, it seems to affect the nucleation rate of small pores obtained through the mechanism A. The kinetics of growth for the majority of individual pores can be described using an exponential-like function. This kinetics is faster for mechanism B compared to mechanism A.

Graphical abstract

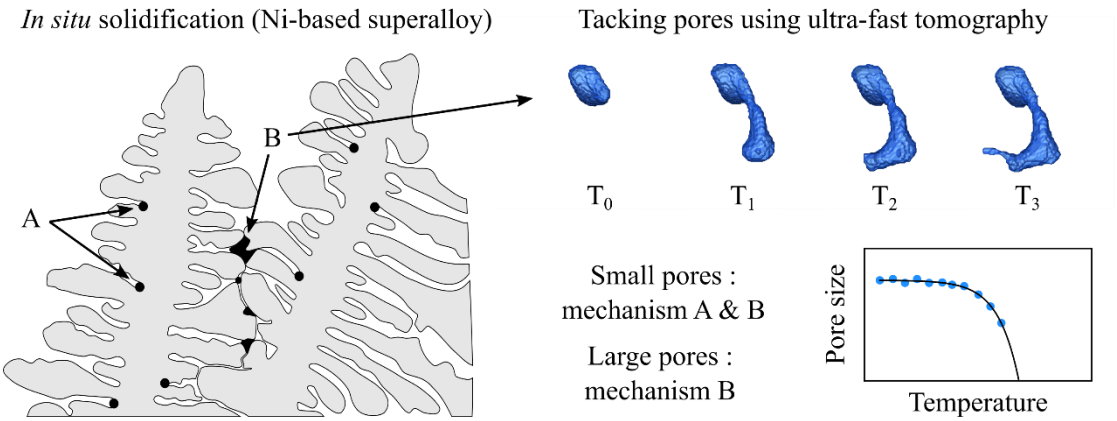

Keywords

Porosity; In situ; Solidification; Time-resolved microtomography, Nucleation; Growth; Superalloys

1. Introduction

The control of shrinkage porosity in cast nickel-based superalloys is essential to extend the service life of jet engine components being operated at high-temperature under cyclic loads. Casting defects such as shrinkage pores are well-known nucleation sites for microcracks in low cycle fatigue [1,2] as well as in high cycle fatigue [3]. Defect sizes ranging from a few microns to several hundreds of microns can affect fatigue properties but the largest defect is often considered as the key parameter that governs the fatigue resistance. Shrinkage pores also act as internal sinks for vacancies during creep deformation [4]. They can grow significantly to adopt a polyhedral shape and eventually contribute to extensive creep cavitation before failure [5]. In the late stages of creep, large pores are known to be nucleation sites for micro-crack as well [6,7].

The size, shape and distribution of casting pores in the microstructure are influential factors for fatigue and creep resistance. Typically, larger pores (of the order of few hundreds of microns) tend to promote stress concentration and pores with irregular shapes can encourage crack nucleation through notch-like effects. As an illustration, the creep resistance of superalloys below 1000°C can be improved significantly when the size and density of pores is decreased by hot isostatic pressing [8]. Also, fatigue life improvements in the low cycle regime, attributed to refined porosity, have been reported in single crystals [9]. Undoubtedly, it is of fundamental interest to understand the mechanisms leading to pores with contrasted sizes and shapes during solidification and to assess the effect of key processing parameters, such as the cooling rate, on their final characteristics.

X-ray micro-tomography is a suited characterization tool to investigate porosity in millimeter-sized samples. It provides a 3D description of the sample internal structure, with a micrometer spatial resolution and with a high acquisition rate when performed at synchrotron radiation facilities [10]. Microtomography has been employed to investigate the pore population in superalloy single crystals, in relation with their chemical composition and processing parameters [11–13], and creep resistance [7,11]. Through *ex situ* measurements, only limited information can be gathered on pore formation and growth mechanisms occurring during solidification. *In situ* X-ray radiography first provided time-resolved insights into the phenomenon [14,15]. However, the recent introduction of CMOS cameras with ultra-fast acquisition rates has enabled the *in situ* monitoring of solidification processes [16–18]. This technological leap has been used to further investigate, for example, dendritic growth in model alloy systems, typically Al-Cu, showing a strong absorption contrast between the copper-enriched liquid and the solid phase [17,19–21]. Similarly, Hf-bearing alloys have been used to

study Ni, Fe and Co binary systems with a high melting temperature [22]. In those peculiar cases, the 3D morphology of the dendrites could be tracked accurately and the fraction of solid estimated because the absorption contrast between the liquid and the solid phase was pronounced. Thus mechanisms such as dendrite growth and coalescence were characterized.

In this work, real-time *in situ* "4D" microtomography was employed to track the formation and growth of individual pores during solidification of a commercial nickel-based superalloy. Three cooling rates were investigated (0.1°C/s, 0.5°C/s and 1°C/s) to evaluate the effect of this key processing parameter on the formation of porosity. Phase contrast obtained with a coherent X-ray beam was used in order to visualize the evolution of corresponding dendritic structures because of the absence of sufficient absorption contrast. The mechanisms leading to two populations of pores with contrasted final characteristics, namely size and shape were identified. For the first time, the kinetics of pore nucleation and growth during solidification of a commercial Ni-based superalloy, depending on the cooling rate, is reported and discussed in relation to the resulting pore size and morphology.

2. Experimental methods

2.1. Samples

The material investigated was an industrial grade Ni-based superalloy containing substantial amount of Co, Cr and Mo, a combined amount of Ti and Al of 8.6 wt% and traces of B. Its detailed chemical composition is proprietary and cannot be reported here. More details can be found in references [23–25], in particular in [25] where the contents of the main alloying elements are provided. The raw material was machined into cylindrical samples with a pin extending over a base, as shown in **Figure 1a**. The pin corresponded to the area being melted and solidified during the experiment and was therefore probed with X-ray microtomography. It had a diameter of 0.8 mm and a height of 1.6 mm. The cylindrical base had a 4.5 mm diameter wide, a 5 mm height and featured a small hole designed to receive a thermocouple used to monitor the temperature during the experiment, in the immediate vicinity of the pin.

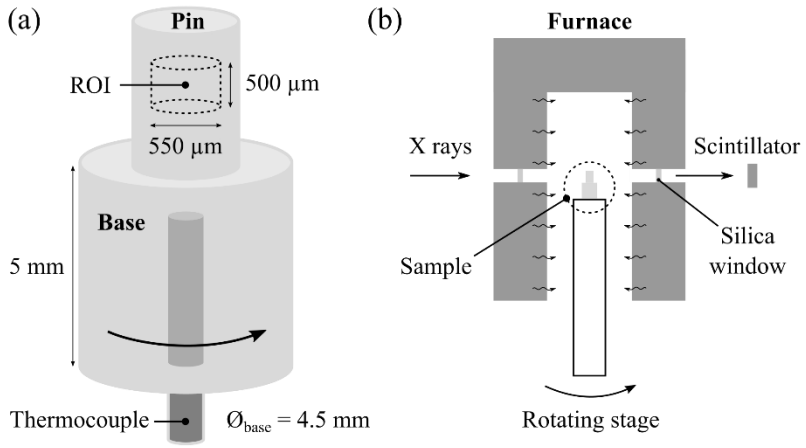

Figure 1. Overview of the setup used to perform in situ solidification experiments. (a) Schematic of the sample geometry. The region of interest (ROI) is located at the center of the pin (top part of the sample). A thermocouple was inserted in the base of the sample to monitor the temperature close to the ROI. (b) A furnace compatible with in situ time-resolved microtomography acquisitions was used to control the cooling rate of the sample.

2.2. In situ solidification

Solidification experiments were performed *in situ* on the micro-tomography setup available at beamline ID19 of ESRF. Prior to each solidification experiment, a sample was glued onto a tall alumina rod attached to a Leuven fast rotating stage. The sample was first melted in a resistive furnace specifically designed for samples with a millimetric size (courtesy of *Mines ParisTech* [19]) and then cooled down under controlled conditions within the furnace. A thin surface layer of oxide formed during the heating step and acted as a crucible. The furnace was equipped with two thin silica windows allowing to perform microtomography acquisitions all through the experiment (*see* **Figure 1b**). Three cooling rates were investigated: 0.1°C/s (5°C.min^{-1}), 0.5°C/s (28 °C.min^{-1}) and 1°C/s (62 °C.min^{-1}).

Time-resolved microtomography measurements were performed with a pink beam set at a mean energy of 57 keV. A dedicated optical system with a 100µm-thick LuAG scintillator and a x10 Mitutoyo objective lens was placed in front a PCO Dimax CMOS camera dedicated to fast recording. Each acquisition was completed under 3s by taking 750 projections over 180°, and repeated every 12s to 18s depending on the cooling rate. The pixel size in the image was 1.22 µm. The region of interest considered was a cylindrical volume of 0.12 mm^3, taken at the center of the pin, with a diameter of 550 µm and a height of 500 µm (see **Figure 1a**). The volume reconstruction was performed with a filtered back-projection algorithm, applying a correction for ring artefacts, in the software PyHST [26]. Phase contrast was retrieved with a Paganin method [27] set with a δ/β coefficient of 300, δ being the refractivity index and β the absorption contrast.

A type S thermocouple, inserted in the base of the sample, was used to monitor continuously the temperature in the close proximity to the pin. To compensate for small systematic errors in the measurement, the temperature profile was shifted to read 1350°C (a value corresponding to the liquidus temperature for the investigated superalloy, see [22,24]) at time t_0 when solidification started. Time t_0 was chosen as the time during cooling of the last tomography scan showing a fully-liquid region of interest (*i.e.* no dendrites). The uncertainty on the temperature measurement is evaluated below 12°C, the later value being related to the temperature change recorded between two successive microtomography acquisitions at the fastest cooling rate (1°C/s).

2.3. Data processing and tracking method

For each sample, a dataset of 17 acquisitions was selected at given temperatures distributed between 1350°C, at which the sample was fully liquid, and 1150°C, at which the sample was fully-solidified. In each dataset, a drift correction was employed to compensate the displacement of the region of interest (between two reconstructed volumes) associated with the thermal contraction of the sample holder. A registration algorithm was employed to calculate the rigid translation with a pixel accuracy, using the oxide layer as a stable source of contrast. A background subtraction was also carried out to remove long-range intensity gradients in the volume. For quantitative analysis of porosity, straightforward thresholding was performed based on the high contrast between (dark-looking) pores and the dense (liquid or solid) phase.

To track the evolution of individual pores in a dataset, a cross-volume labelling method was developed. First, a volume containing "virtual" pores was generated as an aggregation of all acquisitions over the full temperature range. Virtual pores represent an imprint of the size and shape the actual pores have occupied at different time during solidification, around a fixed position. Each actual pore in the dataset could then be associated with the virtual pore containing its center of gravity and labelled accordingly. Tortuous pores not containing their own center of gravity were associated to the closest virtual pore. This method was found very effective and random assessments did not reveal a significant number of mislabeling. Pores with a volume below 9 voxels were not considered in the quantitative analysis and so were excluded pores in contact with the edge of the cylinder delimiting the region of interest. The resolution limit set to 9 voxels corresponds to a 3D-cross whose maximum dimensions along X, Y and Z are equal to 3 adjacent voxels. With a pixel size of 1.22μm, this means a resolution of 3.66μm. In other words, pores having an equivalent diameter smaller than 3.66μm have been

discarded from our analysis. The sphericity index used in this work was defined as the ratio of the pore volume over the volume of a sphere with the same surface area as the pore. Image processing was performed with the platform Fiji [28] (ImageJ) and 3D views were obtained with the commercial software Avizo.

3. Results and discussion

3.1. Impact of cooling conditions on the residual porosity

The typical morphology of dendritic structures at the three imposed cooling rates is illustrated in **Figure 2a-c**. Cross sections were selected at about 1340°C for intermediate solid fractions. In those images, bright pixels are associated with the solid phase while dark grey pixels correspond to the liquid phase. Phase contrast was used to reveal the dendritic structures because absorption contrast was insufficiently pronounced in this commercial Ni-base superalloy. A weak absorption contrast is a direct consequence of the partitioning of alloying elements during solidification that, on average, gives a similar atomic number within the liquid phase and solid phase respectively. As a result, an accurate and automated estimation of solid fractions was not possible in our experiment. Hence only rough estimations based on 2D cross sections, are provided as reference in **Figure 2**. Note that the solid fraction estimation given for a cooling rate of 0.1°C/s might not be reliable as the volume of region of interest is limited relative to the secondary dendrite arm spacing. In **Figure 2a-c**, a schematic associated with each 2D view highlights the dendrites size and morphology.

An estimation of the secondary arm spacing λ_2, carried out at high solid fraction and for a temperature of 1290°C, is also presented in **Table 1**. The values measured are consistent with those reported for nickel-based superalloys in reference [29] and show that a satisfactory control of the cooling conditions was achieved in our experiments. As expected, finer dendritic structures are obtained at faster cooling rates. However, one should notice that we do not see a drastic variation of the secondary arm spacing given the range of cooling rates investigated. More significant differences would be observed if varying the cooling rates by several order of magnitude. At 1°C/s and 0.5°C/s (**Figure 2b** and **Figure 2c**), a full dendrite can be identified in the 2D cross sections, with a trunk and secondary arms. Other features suggest the presence of surrounding dendrites with different orientations. This observation was confirmed by inspecting the whole volume from several angles. At 0.1°C/s, only large secondary dendrite arms are observed, see **Figure 2a**. In this case, the volume investigated using X-ray microtomography does not fully capture the coarse nature of the dendrite structure. To avoid a representativeness bias, this last dataset is not considered hereafter for porosity-related investigations.

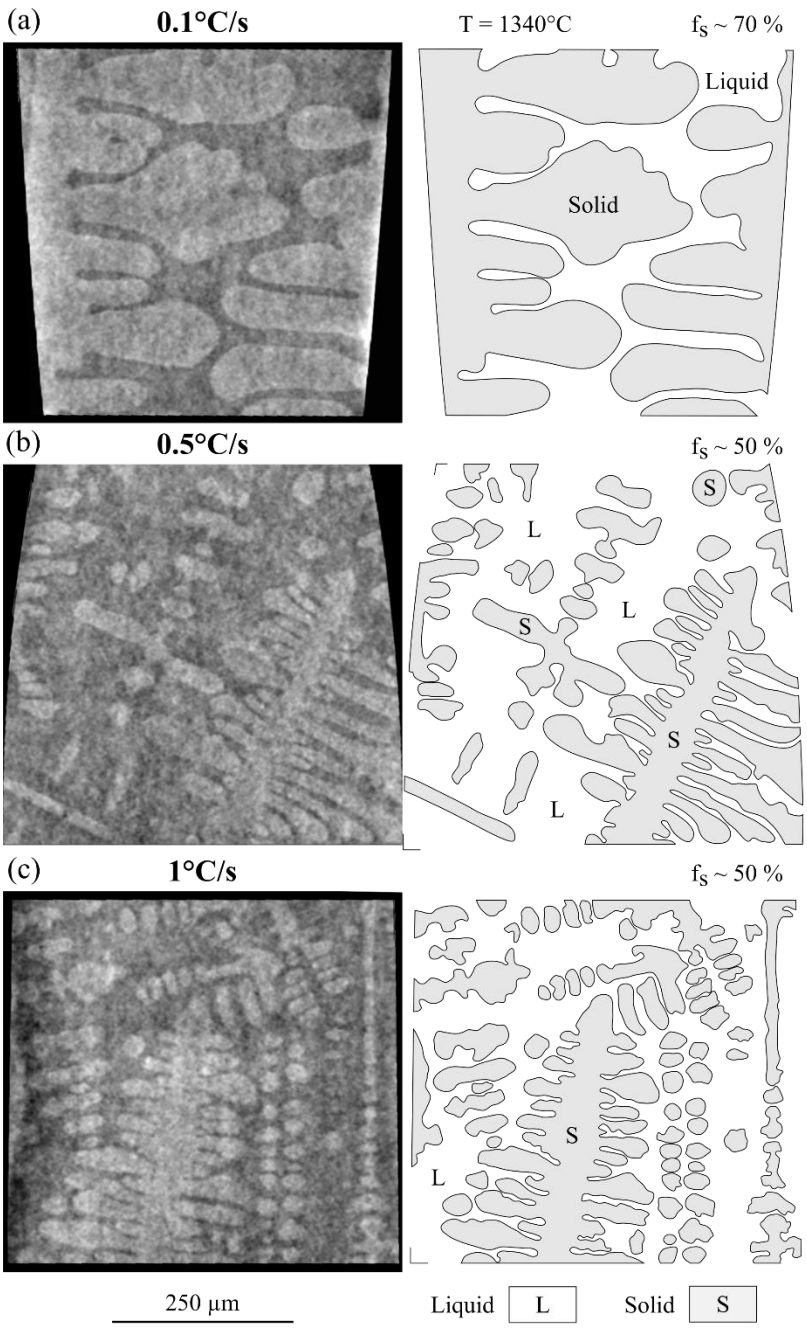

Figure 2. Dendritic solidification structures observed at 1340°C for three cooling rates: (a) 0.1°C/s, (b) 0.5°C/s and (c) 1°C/s. For each sample, a slice of the reconstructed volume is shown (left). For a sake of clarity, a schematic is provided to illustrate the distribution of liquid and solid phases (right) along with a rough estimation of the average solid fraction f_s as quantified on cross sections. Note that the solid fraction estimation given for a cooling rate of 0.1°C/s might not be reliable as the volume of region of interest is limited.

Cooling rate	0.1°/s	0.5°/s	1°/s
λ_2 for $f_s > \sim 95\%$	$> 110\ \mu m$	$\sim 70\ \mu m$	$\sim 50\ \mu m$

Table 1. Secondary dendrite arm spacing estimated at 1290°C, after dendritic growth and coalescence.

The porosity observed once solidification is completed, in the samples with fine dendritic structures, *i.e.* cooled down at 0.5°C/s and 1°C/s, is shown in **Figure 3a** and **Figure 3b**. The pore volume fraction is estimated at 0.22% for a cooling rate of 0.5°C/s and 0.14% for a cooling rate of 1°C/s. The pores density, however, is found higher at 1°C/s (7800 pore/mm^3) than at 0.5°C/s (5500 pore/mm^3), it means 30% more pores when the cooling rate is doubled. As illustrated in the 2D histograms shown in **Figure 3c** and **Figure 3d**, the majority of pores in both samples have an equivalent diameter below 10µm with a round shape leading to sphericity indices higher than ~0.8. Larger pores tend to be more tortuous and are associated with lower sphericity indices.

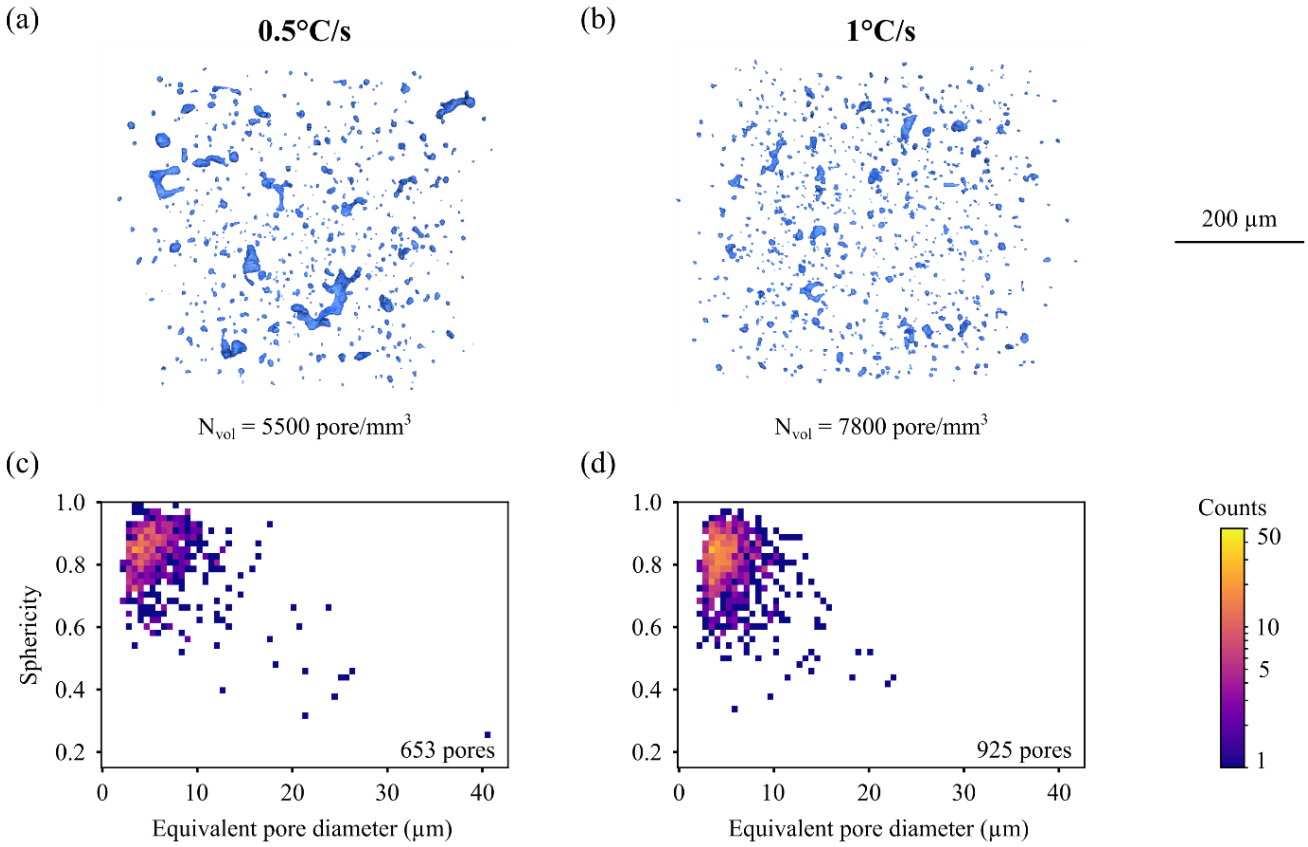

Figure 3. 3D view of the porosity after complete solidification for two cooling rates: (a) 0.5°C/s and (b) 1°C/s. Associated 2D histograms providing a characterization of the pore population in terms of size and sphericity for a cooling rate of (c) 0.5°C/s and (d) 1°C/s.

At higher cooling rate, the porosity features more pores of smaller size. For example, the largest pore for a cooling rate of 1°C/s has an equivalent diameter of 23 µm while it is 40 µm for a cooling rate of 0.5°C/s. This general observation is also in agreement with the refined dendritic structure shown in **Figure 2c**.

3.2. Partitioning the pore population

A distinction is made in **Figure 4a** between two populations of pores with contrasted final characteristics: namely small pores (**Figure 4b**) and large pores (**Figure 4c**) and. The distinction is made because large pores, in average more tortuous, are expected to impact the creep and fatigue behavior significantly more than smaller, rounder pores. As seen in **Figure 4**, pores having a sphericity below 0.5 will be defined as large pores. Such a threshold based on sphericity corresponds to a critical pore equivalent diameter of about 9µm.

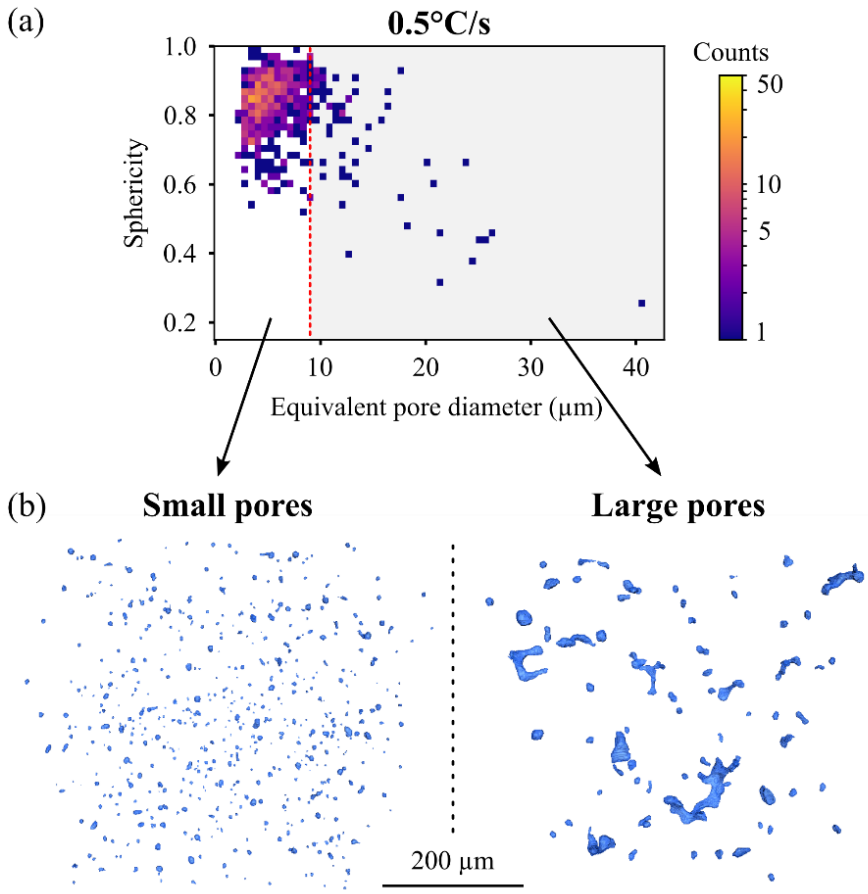

Figure 4. Partitioning the pore population into small pores and large pores illustrated sample cooled at 0.5°C/s. (a) Position of the threshold and (b) 3D renderings of the two subpopulations.

As shown in **Figure 5**, for a cooling rate of 0.5°C/s, large pores are generated between 1250°C and 1200°C while small pores are created from 1325°C to 1175°C. This difference suggests that different mechanisms of pore formation and growth are activated during cooling. The two mechanisms identified in our experiment are discussed in the following section.

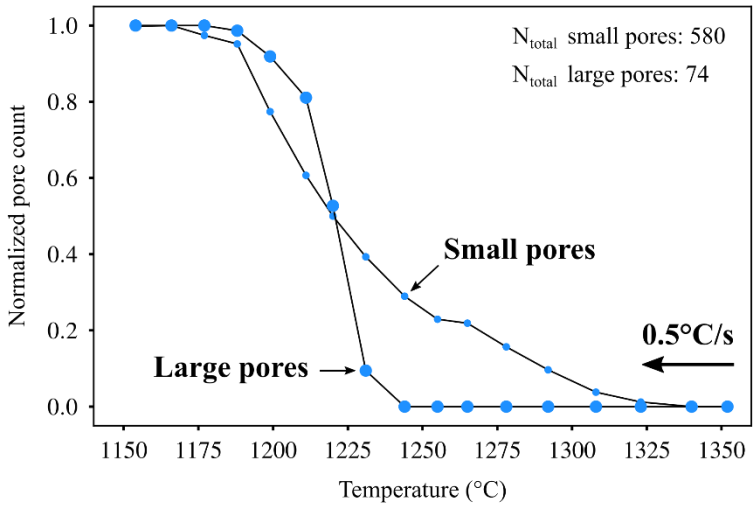

Figure 5. Normalized count of small pores and large pores during solidification at a cooling rate of 0.5°C/s. All curves are normalized by the total number of pores (N_{total}) observed after complete solidification (T ≈ 1150°C).

3.3. Mechanisms of pore formation

3.3.1. Mechanism A: porosity between secondary dendrite arms

The first mechanism (mechanism A) is illustrated in **Figure 6**. 2D cross sections shown in **Figure 6a** and selected in the growth plane of a single dendrite, reveal how small pores are being formed in between secondary dendrite arms due to insufficient liquid flow perpendicularly to the primary dendrite trunks. This insufficient liquid feeding in between dendrite secondary arms is caused by secondary arms coalescence. At 1340°C, a typical dendritic morphology is observed, featuring a trunk and secondary arms extending from both sides. At 1320°C, secondary arms appear significantly larger and in smaller number, a result of growth and coalescence of the dendrite arms. At 1290°C, residual liquid films are the last traces of the tree-shape morphology in the almost fully solidified dendrite. As pointed out by the arrows, small pores appear near the trunk of the dendrite, at positions matching liquid films observed at higher temperature between secondary arms. In the orthogonal view taken slightly away from the trunk (**Figure 6b**), it can be seen that pores are created with a round shape and are always located in the middle of the secondary arm alignment.

Mechanism A can be described by considering the decrease of liquid flow between secondary dendrite arms due to the coalescence of secondary dendrite arms at high temperature. As described by Mortensen [30] and later observed *in situ* in other alloy systems [19], the coalescence of two dendrite arms can lead to a pocket of residual

liquid close to the trunk. This pocket is almost isolated from the liquid remaining in the interdendritic space and may evolve into a shrinkage-like pore. Because the characteristic size of the pocket is close to the thickness of the liquid film before coalescence, only small pores can be created through mechanism A. Pockets of liquid tend to adopt a rather round morphology, in relation with the progressive nature of the growth, so that pores created tend to have a high sphericity. Additionally, an average rough estimate of the local solid fraction at 1340°C, performed on various 2D slices extracted from the reconstructed volume, lead to a value of 0.6 which seems a reasonable fraction according to Mortensen [30] to observe the first secondary dendrite arm coalescence events.

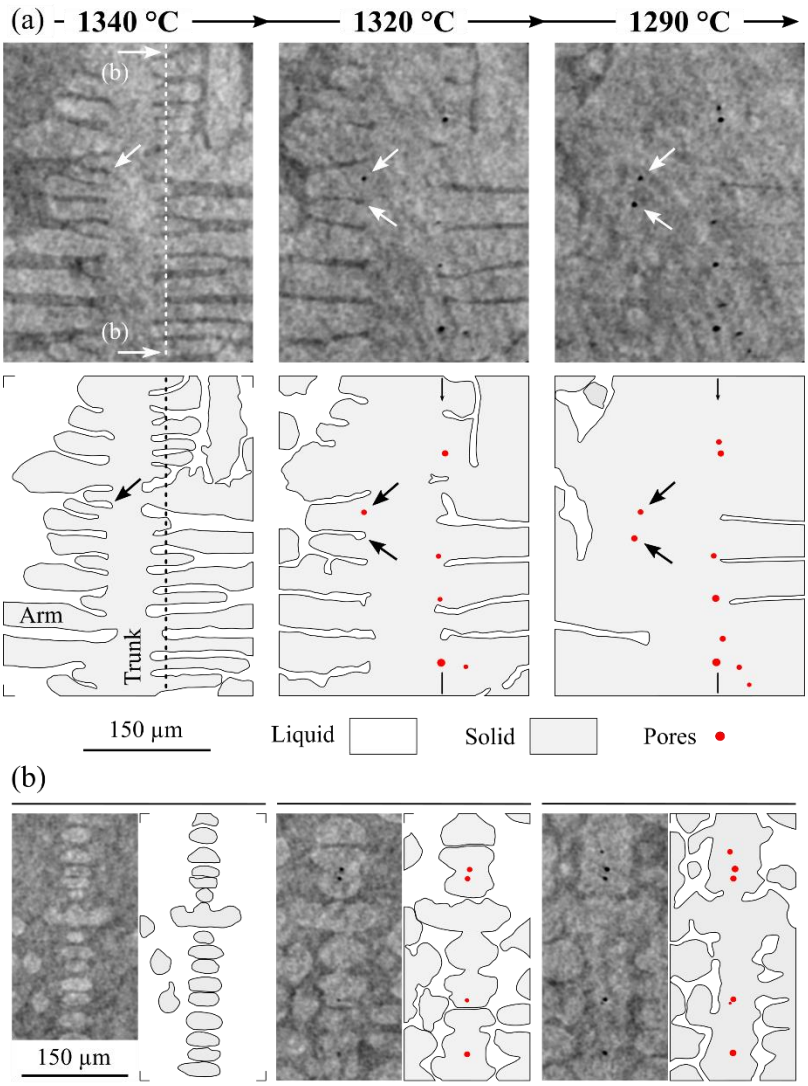

Figure 6. Mechanism A – Formation of small pores at high temperature induced by growth and coalescence of secondary dendrite arms (here for a cooling rate of 0.5°C/s). (a) 2D cross sections extracted at different temperatures showing the creation of pores within the regions containing residual liquid films, between two secondary arms before coalescence (arrows). (b) Orthogonal view of the dendrite arms, taken along the dotted line indicated in (a), suggesting that residual pockets

of liquid are being entrapped close to the trunk and between two dendrite arms as a result of coalescence, leading to the formation of a small pore.

3.3.2. Mechanism B: porosity in the interdendritic space

The characteristics of the second mechanism (mechanism B) are illustrated in **Figure 7**. 2D cross sections extracted from X-ray tomography 3D reconstructed volume show the evolution of interdendritic regions during the last stages of solidification. At 1290°C, the large solid areas are associated with dendritic structures after substantial growth and coalescence (see **Figure 6**). The residual liquid indicates interdendritic regions where solidification happens last. At 1230°C, a uniform contrast is observed indicating near-complete solidification. At 1220°C, a large pore is formed at a position previously occupied by interdendritic liquid. As seen on the 3D rendering in **Figure 7b**, the pore initially round grows significantly in size and adopt a more tortuous shape.

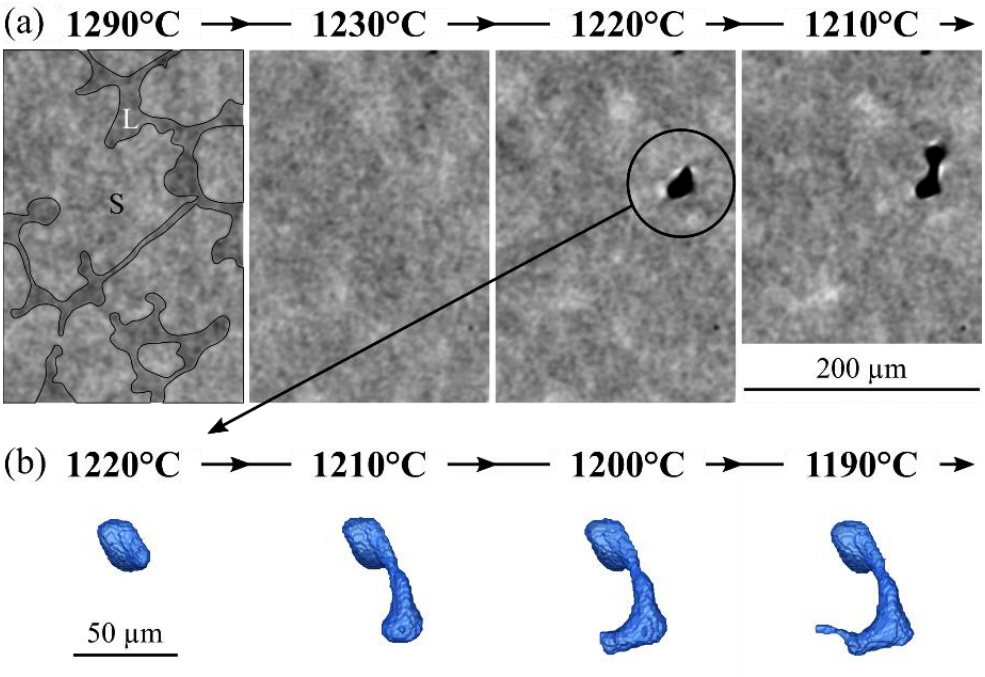

Figure 7. Mechanism B – Formation of pores at intermediate and low temperature in the interdendritic space (here for a cooling rate of 0.5°C/s). (a) Evolution of a single cross section showing the apparition of a pore after apparent complete solidification. (b) 3D rendering of the pore showing the growth mechanism during the last stages of the solidification process.

Mechanism B is typical of shrinkage porosity generated by insufficient liquid feeding in the interdendritic space during the last stages of solidification and promoted by thermal contraction [31]. As expected, this mechanism is activated mostly at low temperature (1220°C in the example shown in **Figure 7**), in the last stages of solidification. In **Figure 7a**, thin films of residual liquid are likely

stables down to 1190°C, although the spatial resolution and sensitivity of our analysis is insufficient to detect them. The presence of residual liquid is required to support the growth mechanism taking place in-between dendrites. We observed that Mechanism B can lead to large pores with tortuous shapes, as shown in **Figure 7b**, as well as small pores with a spherical-like shape. The size and shape of the pore depend mostly on the local geometrical and topological configuration of the interdendritic volume and on the surrounding liquid feeding conditions.

3.4. Effect of cooling rate on pore nucleation

The evolution of the normalized number of small pores and large pores is reported in **Figure 8a** and **Figure 8b** respectively for two cooling rates: 0.5°C/s and 1°C/s. Large pores are formed in a relatively narrow temperature range, roughly between 1230°C and 1200°C, and the nucleation rate appears similar for both cooling rates (see **Figure 8b**). In contrast, small pores are generated in a wide range of temperature, between 1320°C and 1180°C, and the kinetics of nucleation seems to be sensitive ~~depend significantly on~~ the cooling rate (see **Figure 8a**). At slower cooling rates, a higher number of small pores are generated at higher temperature: for example, 20% of the final pore count is reached at 1270°C for a cooling rate of 0.5°C/s while this value is reached at 1230°C for a cooling rate of 1°C/s.

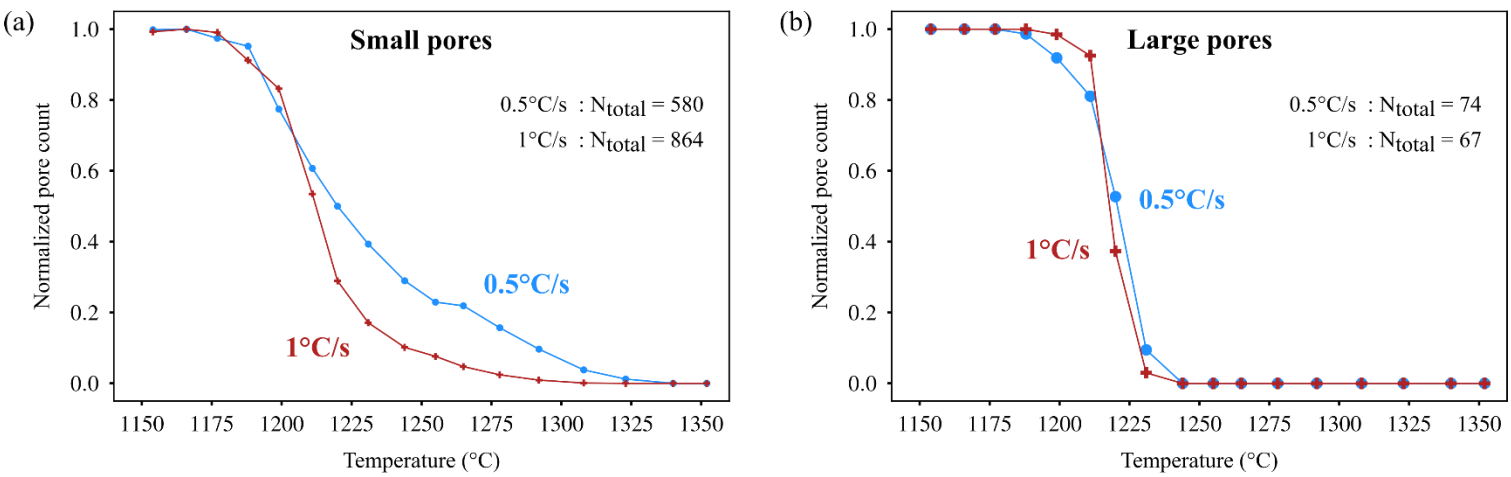

Figure 8. Evolution of the normalized number of (a) small pores and (b) large pores during solidification at a cooling rate of 0.5°C/s and 1°C/s. All curves are normalized by the total number of pores (N_{total}) observed after complete solidification ($T \approx 1150°C$).

The kinetics of nucleation is consistent with the two mechanisms identified. Large pores are obtained through mechanism B at the end of solidification only. On the contrary, small pores are created by

both mechanisms, i.e. at high temperature through mechanism A and at lower temperature through mechanism B.

Our purpose is now to make a deconvolution between the two mechanisms for the generation of small pores because both mechanisms A and B contribute to the formation of small pores. This should help to determine characteristic temperatures for the nucleation of small pores through each individual mechanism. To do so, a simple model is introduced below to further comment on the effect of the cooling rate on the nucleation of small pores. Both mechanism A and mechanism B are assumed to follow a Gaussian nucleation rate as suggested by equation (1).

$$\dot{N} \propto \frac{1}{\sigma\sqrt{2\pi}} e^{-\frac{(T-\mu)^2}{2\sigma^2}} \qquad (1)$$

In equation (1), μ is the mean and σ is the standard deviation of the Gaussian distribution. The total number of pores created is the sum of both mechanisms. Relying on previous hypotheses, a least-square fit was performed for the two cooling rates investigated (0.5 and 1°C/s) and the parameters for the nucleation rates identified. The result are presented in **Figure 9a-b** while the mean value μ and the standard deviation σ for each mechanisms are reported in **Table 2**.

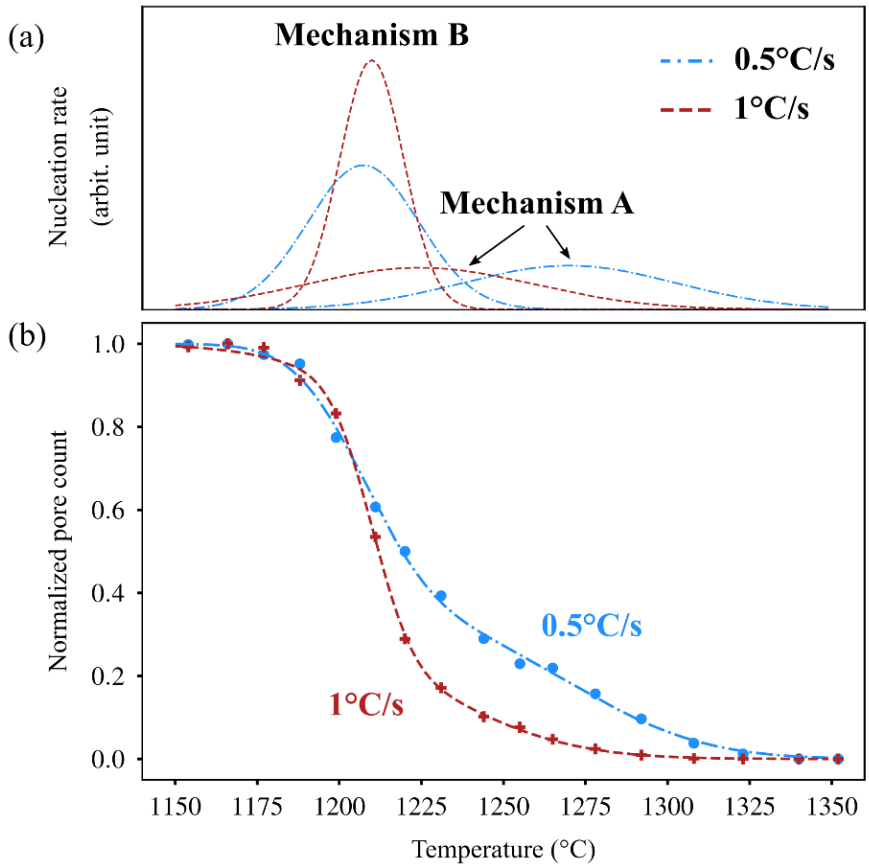

Figure 9. The evolution of the number of small pores is separated into contributions from mechanism A and mechanism B. A gaussian nucleation rate was assumed for both mechanisms and the resulting least-square fit performed with the experimental pore counts is shown.

	Mechanism A		Mechanism B	
	μ_A	σ_A	μ_B	σ_B
0.5 °C/s	1270°C	32°C	1207°C	17°C
1 °C/s	1225°C	34°C	1210°C	10°C

Table 2. Mean values μ and standard deviations σ of the Gaussian nucleation rates identified during the deconvolution process of small pores shown in Figure 9.

On the one hand, mechanism B does not seem sensitive to the cooling rate as shown by relatively similar mean values and standard deviations. This is in agreement with the observation made on the large pore population (created only through mechanism B) with a mean value found to be about 1220°C. On the other hand, our analysis suggests that mechanism A depends ~~significantly~~ on the cooling rate though the cooling rate was just doubled. The mean

value for the deconvolution is found to be 1270°C for a cooling rate of 0.5°C/s whereas it is only 1225°C for a cooling rate of 1°C/s.

To summarize, we believe that both mechanism A and mechanism B are shrinkage-type of porosity triggered by similar fundamental causes, such as insufficient liquid feeding in confined areas, although the local conditions suitable for a pore nucleation differs between the two mechanisms. The development of favorable local conditions, i.e. limited liquid feeding, explains the contrasted sensitivity of mechanism A and mechanism B to the cooling rate. First, note that the nucleation of gas pores is unlikely to happen here as the difference of hydrogen solubility between the liquid and the solid phase is relatively limited in Ni-based alloys [32] contrary to what is reported for Al-alloys where gas pores have often been reported, see e.g. [15,30]. Second, we did not observe spherical pores in the liquid at high temperature during the early stages of solidification.

As stated before, mechanism A is strongly linked with the coalescence of secondary dendrite arms since it reduces liquid flow normal to the primary dendrite trunks. Close to the dendrite trunk, around residual pockets of liquid, conditions to ensure a proper liquid feeding in-betweeen dendrite secondary arms are not fulfilled anymore (strong decrease of the permeability for flow perpendicularly to the primary trunks due to secondary arms coalesecence), even if the overall solid fraction is still relatively low (~60%). Thus mechanism A depends on secondary arm coarsening, a phenomenon which occurs during the early stages of solidification and which starts earlier, i.e. at higher temperature when the cooling rate is divided by a factor 2, see [33].

Mechanism B is governed by the permeability of the dendritic structures for flow parallel to primary trunks during the last stages of solidification, at large overall solid fractions, typically when f_S>90%. Ganesan *et al.* [34] have studied the permeability (denoted K) for flow parallel to primary dendrites arms and they derived an analytical equation linking the permeability to the primary dendrite arm spacing (denoted λ_1), the fraction of liquid (denoted f_L, hence solid f_S) and other geometrical parameters. This equation shows that the permeability K for flow parallel to primary dendrite arms, which is thought to be the root cause of pores forming through mechanism B, is proportional to λ_1^2. The fact that mechanism B is not significantly sensitive when the cooling rate changes from 0.5°C/s to 1°C/s, contrary to mechanism A, can be rationalized. Indeed, we first estimated the primary dendrite arm spacing λ_1 on 2D cross sections, see typically **Figure 2**, for samples cooled at 0.5°C/s to 1°C/s. Our rough estimation of λ_1 gives: λ_1 (0.5°C/s) ≈ 200-300µm and λ_1 (1°C/s) ≈ 150-200µm are consistent with the ones reported in reference [28] which has reviewed the results obtained in many different studies. Thus doubling the cooling rate does not lead to a drastic change of

the primary dendrite arm spacing, therefore such a variation does not sufficiently change the permeability values to alter the sensitivity of mechanism B to cooling rate change, at least in the range explored in the present work. Mechanism B is thus less sensitive to limited variations of cooling rate than mechanism A.

3.5. Effect of cooling rate on pore growth

The kinetics of growth was evaluated with the tracking method described in section 2.3 for each pore with a final equivalent diameter larger than 6µm. For pores with a smaller final diameter, the spatial resolution of our analysis was considered insufficient to monitor the process. As illustrated in **Figure 10**, the kinetics of growth can vary significantly from pore to pore. We found that equation (2) could be used to fit efficiently the majority of the experimental data.

$$D_{eq}^{n} = 1 - e^{\alpha(T-T_0)} \tag{2}$$

where D_{eq}^{n} is the normalized equivalent diameter, T_0 is the nucleation temperature and α is a parameter governing the kinetics of pore growth. 40% of the pores are detected directly with their final size or, alternatively, only a single point is available to fit their size evolution (see typically cases where $\alpha = 0.3$ in **Figure 10**). In such cases, the temporal resolution of our analysis was deemed insufficient to robustly describe the kinetics of pore growth and the associated pores were not considered further in the analysis.

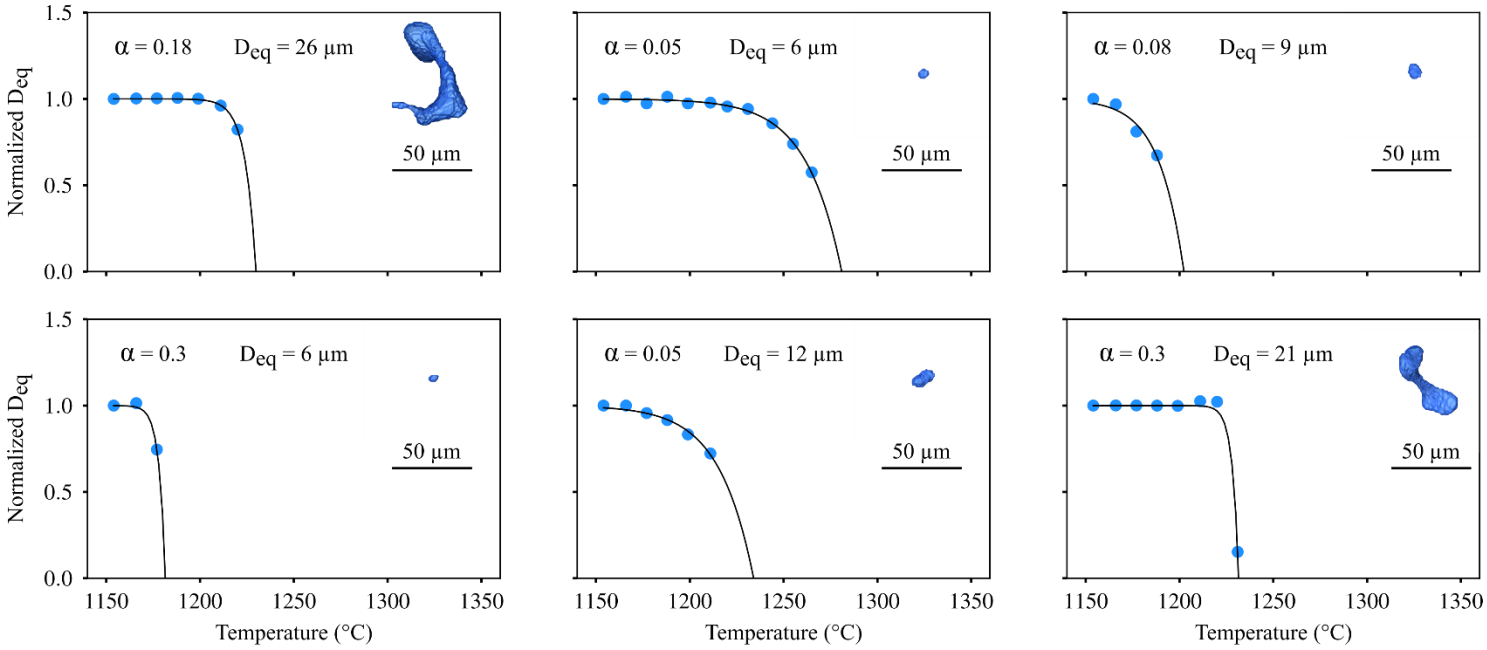

Figure 10. Illustration of the tracking method used to monitor the growth of individual pores. An exponential-like function with two parameters was fitted to the

data to provide a parametric description of growth. A 3D rendering of individual pores in their final shape is also shown.

A plot of the coefficients fitted for 256 pores (60% of the total population) is provided in **Figure 11** for two cooling rates. Each dot in **Figure 11** has a size proportional to the final equivalent diameter of the pore. As discussed above, large pores nucleate in a narrow band of temperature compared to small pores. No apparent correlation is detected between the final size of the pore and the α coefficient. For both cooling rates, we see that small pores nucleating at high temperature (roughly > 1250°C) have low α coefficient, typically below 0.1. At lower temperatures, a large dispersion in the values of α is observed in a range between 0.05 and 0.3. As the temperature decreases, we see a tendency to observe higher coefficients. This suggests that pore growth is faster, in average, for mechanism B than mechanism A.

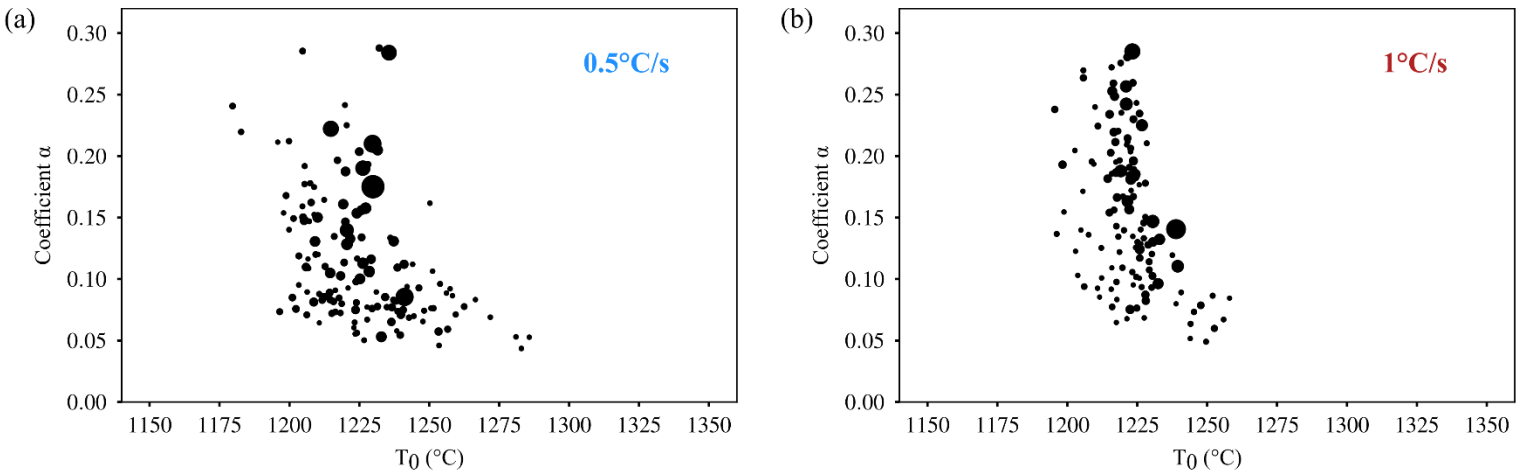

Figure 11. Distribution of parameters α and T_0 from equation (1), fitted on individual pores using the tracking method, for two cooling rate: (a) 0.5°C/s and (b) 1°C/s. The size of each dot is proportional to the final equivalent diameter of the pore.

Among the population of pores considered in our growth analysis, at higher cooling rate, the growth seems faster on average: the mean value of α is 0.18 for a cooling rate of 1°C/s but it is only 0.13 for a cooling rate of 0.5°C/s. Overall, it appears that the distribution of parameters describing pore growth is ~~significantly~~ affected by the cooling rate considered., even within the restricted range of cooling rate considered in the present work.

4. Conclusions

Based on the work reported above, the following conclusions can be drawn:

- Time-resolved *in situ* microtomography can be used to track the nucleation and growth of individual pores during solidification of industrial-grade Ni-based superalloys at representative cooling rates (1°C/s).
- Phase contrast imaging, in the absence of X-ray absorption contrast, provides valuable data on the evolution of dendritic structures during solidification.
- Two mechanisms of pore formation have been identified. Both mechanisms lead to shrinkage pores in confined regions with a high local solid fraction. Mechanism A is associated with the insufficient liquid flow normal to the primary dendrite trunks caused by the coalescence of secondary dendrite arms at temperature above approximately 1220°C. Mechanism B is related to insufficient feeding of the interdendritic space during the last stages of solidification, at lower temperatures.
- Small pores usually exhibit a high sphericity and are generated through both mechanism A and mechanism B in a large range of temperature. Large pores often have a tortuous shape and are formed through mechanism B only, in a narrow range of temperature around 1220°C.
- A variation of the cooling rate by a factor 2 does not affect the nucleation rate of large pores and small pores obtained through mechanism B although it has a significant impact on the nucleation rate of small pores obtained through mechanism A. As the cooling rate decreases, small pores are nucleated at higher temperature.
- The kinetics of individual pore growth has been characterized. This kinetics is faster for mechanism B compared to mechanism A.

Aknowledgements

This work was performed within the framework of the Center of Excellence of Multifunctional Architectured Materials ‘‘CEMAM’’ n°AN-10-LABX-44-01 funded by the ‘‘Investments for the Future Program’’. The European Synchrotron Radiation Facility (ESRF) is gratefully acknowledged for offering beam-time associated to the MA3483 proposal.

References

[1] M.R. Orlov, Pore Formation in Single-Crystal Turbine Rotor Blades during Directional Solidification, 2008 (2008) 56–60. doi:10.1134/S0036029508010114.

[2] K. Prasad, R. Sarkar, K. Gopinath, Role of shrinkage pores , carbides on cyclic deformation behaviour of conventionally cast nickel base superalloy CM247LC s at 870 ° C, 654 (2016) 381–389. doi:10.1016/j.msea.2015.12.054.

[3] L. Kunz, P. Lukáš, R. Konečná, High-cycle fatigue of Ni-base superalloy Inconel 713LC, Int. J. Fatigue. 32 (2010) 908–913. doi:10.1016/j.ijfatigue.2009.02.042.

[4] A. Epishin, T. Link, Mechanisms of high-temperature creep of nickel-based superalloys under low applied stresses, Philos. Mag. 84 (2004) 1979–2000. doi:10.1080/14786430410001663240.

[5] R.C. Reed, Single-crystal superalloys for blade applications, in: The Superalloys, 2009: pp. 121–216. doi:10.1017/cbo9780511541285.005.

[6] H. Buck, P. Wollgramm, A.B. Parsa, G. Eggeler, A quantitative metallographic assessment of the evolution of porosity during processing and creep in single crystal Ni-base super alloys, Materwiss. Werksttech. 46 (2015) 577–590. doi:10.1002/mawe.201500379.

[7] J.B. le Graverend, J. Adrien, J. Cormier, Ex-situ X-ray tomography characterization of porosity during high-temperature creep in a Ni-based single-crystal superalloy: Toward understanding what is damage, Mater. Sci. Eng. A. 695 (2017) 367–378. doi:10.1016/j.msea.2017.03.083.

[8] L. Mujica Roncery, I. Lopez-Galilea, B. Ruttert, D. Bürger, P. Wollgramm, G. Eggeler, W. Theisen, On the Effect of Hot Isostatic Pressing on the Creep Life of a Single Crystal Superalloys, Adv. Eng. Mater. 18 (2016) 1381–1387. doi:10.1002/adem.201600071.

[9] S. Steuer, P. Villechaise, T.M. Pollock, J. Cormier, Benefits of high gradient solidification for creep and low cycle fatigue of AM1 single crystal superalloy, Mater. Sci. Eng. A. 645 (2015) 109–115. doi:10.1016/j.msea.2015.07.045.

[10] L. Salvo, P. Cloetens, E. Maire, S. Zabler, J.J. Blandin, J.Y. Buffière, W. Ludwig, E. Boller, D. Bellet, C. Josserond, X-ray micro-tomography an attractive characterisation technique in materials science, Nucl. Instruments Methods Phys. Res. Sect. B Beam Interact. with Mater. Atoms. 200 (2003) 273–286. doi:10.1016/S0168-583X(02)01689-0.

[11] T. Link, S. Zabler, A. Epishin, A. Haibel, M. Bansal, X. Thibault, Synchrotron tomography of porosity in single-crystal nickel-base superalloys, Mater. Sci. Eng. A. 425 (2006) 47–54. doi:10.1016/j.msea.2006.03.005.

[12] J.L. Liu, J. Meng, J.J. Yu, Y.Z. Zhou, X.F. Sun, Influence of solidification conditions and alloying elements Re and Ti on

micropores formed during homogenization of Ni base single crystal superalloy, J. Alloys Compd. 746 (2018) 428–434. doi:10.1016/j.jallcom.2018.02.221.

[13] K. Matuszewski, H. Matysiak, J. Jaroszewicz, W. De Nolf, K. Kubiak, K.J. Kurzydłowski, Influence of Bridgman process conditions on microstructure and porosity of single crystal Ni-base superalloy CMSX-4, Int. J. Cast Met. Res. 27 (2014) 329–335. doi:10.1179/1743133614y.0000000112.

[14] E.W.J. Miller, J. Beech, In-situ radiographic observations of alloy solidification, Metallography. 5 (1972) 298–300. doi:10.1016/0026-0800(72)90009-2.

[15] P.D. Lee, J.D. Hunt, Hydrogen porosity in directional solidified aluminium-copper alloys: In situ observation, Acta Mater. 45 (1997) 4155–4169. doi:10.1016/S1359-6454(97)00081-5.

[16] L. Salvo, M. Di Michiel, M. Scheel, P. Lhuissier, B. Mireux, M. Suéry, Ultra Fast *In Situ* X-Ray Micro-Tomography: Application to Solidification of Aluminium Alloys, Mater. Sci. Forum. 706–709 (2012) 1713–1718. doi:10.4028/www.scientific.net/msf.706-709.1713.

[17] B. Cai, J. Wang, A. Kao, K. Pericleous, A.B. Phillion, R.C. Atwood, P.D. Lee, 4D synchrotron X-ray tomographic quantification of the transition from cellular to dendrite growth during directional solidification, Acta Mater. 117 (2016) 160–169. doi:10.1016/j.actamat.2016.07.002.

[18] R. Daudin, S. Terzi, P. Lhuissier, J. Tamayo, M. Scheel, N.H. Babu, D.G. Eskin, L. Salvo, Particle-induced morphological modification of Al alloy equiaxed dendrites revealed by sub-second in situ microtomography, Acta Mater. 125 (2017) 303–310. doi:10.1016/j.actamat.2016.12.005.

[19] N. Limodin, L. Salvo, E. Boller, M. Suéry, M. Felberbaum, S. Gaillièbue, K. Madi, In situ and real-time 3-D microtomography investigation of dendritic solidification in an Al-10 wt.% Cu alloy, Acta Mater. 57 (2009) 2300–2310. doi:10.1016/j.actamat.2009.01.035.

[20] N. Limodin, L. Salvo, M. Suéry, M. DiMichiel, In situ investigation by X-ray tomography of the overall and local microstructural changes occurring during partial remelting of an Al-15.8 wt.% Cu alloy, Acta Mater. 55 (2007) 3177–3191. doi:10.1016/j.actamat.2007.01.027.

[21] A.G. Murphy, W.U. Mirihanage, D.J. Browne, R.H. Mathiesen, Equiaxed dendritic solidification and grain refiner potency characterised through in situ X-radiography, Acta Mater. 95 (2015) 83–89. doi:10.1016/j.actamat.2015.04.060.

[22] M.A. Azeem, P.D. Lee, A.B. Phillion, S. Karagadde, P. Rockett, R.C. Atwood, L. Courtois, K.M. Rahman, D. Dye, Revealing dendritic pattern formation in Ni, Fe and Co alloys using synchrotron tomography, Acta Mater. 128 (2017) 241–248. doi:10.1016/j.actamat.2017.02.022.

[23] E. Chauvet, C. Tassin, J.J. Blandin, R. Dendievel, G. Martin,

Producing Ni-base superalloys single crystal by selective electron beam melting, Scr. Mater. 152 (2018) 15–19. doi:10.1016/j.scriptamat.2018.03.041.

[24] E. Chauvet, P. Kontis, E.A. Jägle, B. Gault, D. Raabe, C. Tassin, J.J. Blandin, R. Dendievel, B. Vayre, S. Abed, G. Martin, Hot cracking mechanism affecting a non-weldable Ni-based superalloy produced by selective electron Beam Melting, Acta Mater. 142 (2018) 82–94. doi:10.1016/j.actamat.2017.09.047.

[25] P. Kontis, E. Chauvet, Z. Peng, J. He, A. Kwiatowski da Silva, Dierk Raabe, C. Tassin, J-J. Blandin, S. Abed, R. Dendievel, B. Gault, G. Martin, Atomic-scale grain boundary engineering to overcome hot cracking in additively manufactured superalloys, Acta Mater. 177 (2019) 209-221 https://doi.org/10.1016/j.actamat.2019.07.041.

[26] A. Mirone, E. Brun, E. Gouillart, P. Tafforeau, J. Kieffer, The PyHST2 hybrid distributed code for high speed tomographic reconstruction with iterative reconstruction and a priori knowledge capabilities, Nucl. Instruments Methods Phys. Res. Sect. B Beam Interact. with Mater. Atoms. 324 (2014) 41–48. doi:10.1016/j.nimb.2013.09.030.

[27] D. Paganin, S.C. Mayo, T.E. Gureyev, P.R. Miller, S.W. Wilkins, Simultaneous phase and amplitude extraction from a single defocused image of a homogeneous object, J. Microsc. 206 (2002) 33–40. doi:10.1046/j.1365-2818.2002.01010.x.

[28] J. Schindelin, I. Arganda-Carreras, E. Frise, V. Kaynig, M. Longair, T. Pietzsch, S. Preibisch, C. Rueden, S. Saalfeld, B. Schmid, J.Y. Tinevez, D.J. White, V. Hartenstein, K. Eliceiri, P. Tomancak, A. Cardona, Fiji: An open-source platform for biological-image analysis, Nat. Methods. 9 (2012) 676–682. doi:10.1038/nmeth.2019.

[29] H.S. WHITESELL, L. LI, R.A. OVERFELT, Influence of Solidification Variables on the Dendrite Arm Spacings of Ni-Based Superalloys, Metall. Mater. Trans. B. 31B (2000) 546–551. doi:10.1080/00304947109356052.

[30] A. Mortensen, On the influence of coarsening on microsegregation, Metall. Trans. A. 20 (1989) 247–253. doi:10.1007/BF02670250.

[31] J.A. Dantzig, M. Rappaz, Solidification, 2nd Editio, EPFL Press, 2016. http://www.solidification.org/.

[32] J. Campbell, Complete Casting Handbook: Metal Casting Processes, Metallurgy, Techniques and Design: Second Edition, 2015. doi:10.1016/C2014-0-01548-1.

[33] J.J. Xu, T.M. Wang, J. Zhu, H.L. Xie, T.Q. Xiao, T.J. Li, In situ study on secondary dendrite arm coarsening of Sn–Bi alloy by synchrotron microradiography , Mater. Res. Innov. 15 (2011) 156–159. doi:10.1179/143307511x12998222919155.

[34] S. Ganesan, C.L. Chan, D.R. Poirier, Permeability for flow

parallel to primary dendrite arms, Mater. Sci. Eng. A. 151 (1992) 97–105. doi:10.1016/0921-5093(92)90186-5.